Contents lists available at ScienceDirect

Engineering Analysis with Boundary Elements

High gradient magnetic particle separation in a channel with bifurcations

M. Zadravec [a], M. Hriberšek [a], P. Steinmann [b], J. Ravnik [a,*]

[a] Faculty of Mechanical Engineering, University of Maribor, Smetanova 17, SI-2000 Maribor, Slovenia
[b] University of Erlangen-Nuremberg, Egerlandstrasse 5, D-91058 Erlangen, Germany

ARTICLE INFO

ABSTRACT

Micro particle separation from solid–liquid suspension under the influence of hydrodynamic and magnetic forces in a channel with bifurcation is studied numerically by applying the Boundary Element Method based fluid flow solver. The particle trajectories are computed using the Lagrangian particle tracking, where the forces on particles are computed based on the point particle representation. In the separator due to the bifurcation channel geometry the magnetic particles experience varying Kelvin force as they travel along the channel, although in the same direction the high gradient magnetic field does not change. In this way, the interplay of hydrodynamic and magnetic forces leads to changes in collection efficiency of the separator. A comparison with magnetic separation in the narrow channel design is done and recommendation for optimal choice of fluid flow rate and magnitude of external magnetic field is discussed.

© 2014 Elsevier Ltd. All rights reserved.

1. Introduction

Separation devices are an important part of the majority of process chains. In case of dispersed solid–fluid flow, separation devices frequently exploit particular properties of the solid particles in order to make separations fast and efficient. In general, the gravity force and hydrodynamic forces are used in order to separate solid particles from the fluid phase. A classical Stokes sedimentation velocity suggests that problems arise when very small particles with densities close to the fluid density are encountered, as the sedimentation velocity decreases significantly. In higher Reynolds number flow regimes the situation changes, but not significantly, since hydrodynamic forces scale with the magnitude of the relative velocity between a particle and the fluid. In such cases, novel separation concepts have to be implemented. One of them is to take advantage of differences in magnetic characteristics between the particulate phase and the fluid phase. If we consider water as the fluid phase, particles with magnetic properties can be separated by means of an additional body force, acting on them in a nonuniform magnetic field [1]. The Kelvin body force, describing this effect, becomes important in case of the existence of a high gradient magnetic field, and if the gradient is aligned in a suitable way it is possible to promote separation

efficiency (collection efficiency) of such separation devices. The other possibility is to have a fixed magnetic field and to design the flow field in such a way that the solid particles would be transported into regions of a high gradient of the magnetic field and hence would be subjected to stronger Kelvin forces, promoting separation.

Several high gradient magnetic separation (HGMS) devices have been proposed [2–6] where the magnetic field gradient is achieved by submerging the magnetizable wires in the fluid. The usage of such systems is present in several fields of science, like life sciences, natural sciences, medicine or engineering sciences. In biomedicine, for example, they are used for magnetic separation of labelled cells and other biological entities [7–9]. Furthermore magnetic field gradients in combination with particles with magnetic properties are used for therapeutic drug, gene, radionuclide delivery [10], in radio frequency methods for the catabolism of tumours via hyperthermia or for contrast enhancement agents for magnetic resonance imaging applications. Synthesis of particles with favourable magnetic properties and biological compatibility has also been studied [11–13], finding iron oxides to be suitable.

In this paper we perform a numerical simulation of magnetic particle laden flow in a high gradient magnetic separation devices with bifurcation. We make use of the in-house 3D boundary element method based fluid flow and Lagrangian particle tracking computational algorithm developed by Ravnik et al. [14]. The computational algorithm was developed and tested for a tracking of particles under the influence of hydrodynamic and magnetic

* Corresponding author.
  E-mail addresses: matej.zadravec@um.si (M. Zadravec),
matjaz.hribersek@um.si (M. Hriberšek),
paul.steinmann@ltm.uni-erlangen.de (P. Steinmann), jure.ravnik@um.si (J. Ravnik).

$h_{bif} = h/2; \; l_{bif} = h$ $h_{bif} = h/8; \; l_{bif} = h$
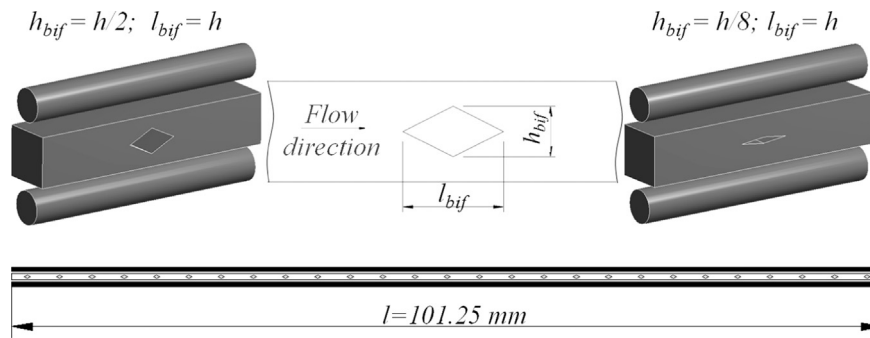

Fig. 1. Geometry of one segment and the whole channel with bifurcating barriers.

forces. It was used to study a HGMS device in a form of a separation channel with a square cross-section and a high aspect ratio, where magnetic field gradient was caused by two magnetized wires placed on the top and the bottom of the channel. The results showed that the derived numerical algorithm for the solution of a dilute suspension flow is capable of accurate solutions of particle motion in a magneto static field problem and consequently suitable to study advanced particle separation devices. A design drawback of such configuration is a stagnation of collection efficiency that can be observed downstream the channel. This is a result of the symmetric distribution of the magnetic forces as well as a symmetric flow field in the cross-section of the channel. After some entry length the particles which are in the central part of the channel are not affected by any magnetic force and are only following the fluid flow.

This paper presents further developments of the computational algorithm and an in-depth study of a modified separation channel with periodic bifurcations. The main goal of the proposed design of the high gradient magnetic separation device was to increase the collection efficiency of particles with the introduction of some perturbations to the flow. The form of bifurcation microfluidic channel with square cross-section geometry was selected. The channel geometry has recently gained attention in studies of blood flow in bifurcating microfluidic tubes and channels [15]. The magnetic field gradient originates from two magnetized wires placed on the top and the bottom of the channel (Fig. 1), the same configuration used in [14], which allowed comparison of the collection efficiency of both channel designs.

2. Problem description

To increase the separation of particles from the bulk fluid flow (collection efficiency of magnetized particles on walls) the geometry of a high gradient magnetic separator in the form of a narrow channel presented in the previous work of Ravnik and Hriberšek [14] was changed to the form of a bifurcation microfluidic channel with a square cross-section geometry. The separation unit consists of a 101.25 mm long square cross section channel (0.75 mm × 0.75 mm) with converging-diverging barriers inside the channel (Fig. 1). Two different barrier heights are chosen: larger $h_{bif} = h/2 = 0.37$ mm and smaller $h_{bif} = h/8 = 0.09375$ mm. The length of the barrier is equal to the channel height $l_{bif} = h = 0.75$ mm. The distance between the barriers is $\Delta l_{bif} = 4h = 3$ mm. The magnetic field is generated by two stainless steel 430 wires of diameter 0.5 mm, which are placed at the top and bottom of the channel and disposed to the homogenous external magnetic field produced by parallel rectangular NdFeB magnets. The considered suspension in this study consisted of dispersed polystyrene magnetic spheres (produced by Micromond Inc.-Germany) with hydrodynamic diameter of $d_p = 1.7$ μm and water

as a fluid at temperature of 20 °C (kinematic viscosity $\nu = 1.01$ mm^2/s and density $\rho_f = 998$ kg/m^3). The composition of the magnetic spherical particles was taken from [16], where dynamic laser scattering in a zeta potential analyser and thermogravimetry analysis was utilized. The spheres contain 12.45% magnetite ($\rho_m = 5000$ kg/m^3) and 87.55% polystyrene ($\rho_{ps} = 1047$ kg/m^3).

The general geometry parameter values of the square cross section channel, water flow rates, magnetic flux densities, and magnetic particle properties are selected in order to replicate a real applicable separation device of a straight channel [16,14], so that a comparison between experimental and numerical analyses can be made. The flow of the water is laminar and its value varies from 27 ml/h to 162 ml/h. These flow rates correspond to average water velocities from $u_0 = 1.35$ cm/s to $u_0 = 8$ cm/s and Reynolds number values from $Re = u_0 h/\nu = 10$ to $Re = 59.36$. In total 10,000 polystyrene magnetic spheres are randomly inserted at the inlet and tracked in the bifurcating channel with different magnetic flux densities varying from $B_0 = 0.04$ T to $B_0 = 0.62$ T. Due to the small flow rates and correspondingly small values of the Reynolds number the flow is laminar and steady state. The suspension is considered as dilute and therefore the assumption of neglecting interaction between the particles is considered. Also the fluid flow and particles are one-way coupled, meaning that the particles are affected by the flow, but the flow is not affected by the particles. The flow is fully developed at the inlet and the particles are randomly distributed across the inlet surface. Due to a high aspect ratio (1:135) the simulation may require large computational times to resolve the fluid field, thus it was divided into 27 shorter segments (Fig. 1). The segments were joined by the means of the periodic boundary condition at the inlet and the outlet of each segment. Values of velocity and vorticity at the outlet are copied back to the inlet plane. Mass flux comparison between inlet and outlet planes is performed. The flow field prescribed on the inlet plane is corrected for small differences in mass fluxes in order to maintain a constant mass flux thought the whole channel. Periodic boundary conditions for the particles are implemented as follows. Particle positions at the outlet are used as inlet positions for simulation of the next segment of the channel. Since there is a bifurcation inside the channel the length of a segment could not be chosen arbitrarily. The length of the segment is chosen in accordance with the demand that after the barrier the flow must regain its fully developed state. For the selected Reynolds number values the 1:5 aspect ratio of the segment is selected and verified regarding the fully developed state of the fluid flow after the barrier.

3. Governing equations

To successfully accomplish the simulation of magnetic particle laden flow in a high gradient magnetic separation device with bifurcation in the channel the first step is the flow computation,

followed by the flow and magnetic field affected computation of particle trajectories inside the separation device.

3.1. Fluid flow

To solve the fluid flow in the framework of the velocity–vorticity formulation of the Navier–Stokes equations and to apply the BEM approximation method, we must first split the dynamics of the flow into its kinematic and kinetic parts. This is done by the use of the derived vector vorticity field function $\vec{\omega}$, obtained as the curl of the compatibility velocity field $\vec{\omega} = \vec{\nabla} \times \vec{u}$. By applying the curl operator to the vorticity and using the mass conservation equation for incompressible fluid flow we obtain an elliptic Poisson equation for the velocity vector:

$$\nabla^2 \vec{u} + \vec{\nabla} \times \vec{\omega} = 0. \tag{1}$$

Eq. (1) represents the kinematic part of the fluid flow where for a known vorticity field $\vec{\omega}$, the corresponding velocity field $\vec{u}$ can be determined. To compute the kinetic part of the flow we apply the curl operator to the momentum conservation equation resulting in the steady vorticity transport equation in the following form:

$$[\vec{u} \cdot \vec{\nabla}]\vec{\omega} = [\vec{\omega} \cdot \vec{\nabla}]\vec{u} + \nu \nabla^2 \vec{\omega}. \tag{2}$$

The boundary conditions for the selected channel flow consist of the known velocities at the inlet, zero velocity flux at the outlet, no-slip velocity boundary condition on channel and barrier walls. Dirichlet type vorticity boundary conditions are applied on all walls, with vorticity values calculated within the flow kinematics part of the BEM computational algorithm.

The Boundary Element Method based computational code [17,18] was used to simulate the flow. The system of Eqs. (1) and (2) is solved in a nonlinear loop consisting of three steps: computation of boundary vorticity values by solving the kinematics equation using the single-domain BEM approach is followed by solving the flow kinematics equation for domain velocities by applying the sub-domain BEM taking into account the newly calculated boundary vorticity values. In the third step, the domain vorticity values are obtained by solving the vorticity transport equation using the sub-domain BEM.

3.1.1. Sub-domain BEM algorithm

To solve kinematic equation (1) by the subdomain BEM approach the whole domain Ω has to be divided into subdomains Ω_i. The boundary of each subdomain is denoted by $\partial\Omega_i$. The integral form of the kinematics equation without derivatives of the velocity and vorticity fields takes the following form:

$$c(\vec{\vartheta})\vec{u}(\vec{\vartheta}) + \int_{\partial\Omega_i} \vec{u}\,\vec{\nabla}u^\star \cdot \vec{n}\,d\Gamma = \int_{\partial\Omega_i} \vec{u}$$
$$\times [\vec{n} \times \vec{\nabla}]u^\star\,d\Gamma + \int_{\Omega_i} [\vec{\omega} \times \vec{\nabla}u^\star]\,d\Omega, \tag{3}$$

where $\vec{r}$ is the field point, $\vec{\vartheta}$ is the source point, $\vec{n}$ is the unit normal to the boundary and $u^\star = 1/4\pi|\vec{\vartheta} - \vec{r}|$ is the fundamental solution of the Laplace operator. The solution of this equation is used in the second step of the BEM algorithm to obtain velocity values inside the computational domain.

The integral form of vorticity transport equation (2) may be written for the jth component of the vorticity vector as [19]

$$c(\vec{\vartheta})\omega_j(\vec{\vartheta}) + \int_{\partial\Omega_i} \omega_j \vec{\nabla}u^* \cdot \vec{n}\,d\Gamma = \int_{\partial\Omega_i} u^* q_j\,d\Gamma$$
$$+ \frac{1}{\nu}\int_{\partial\Omega_i} \vec{n} \cdot \left\{u^*[\vec{\nabla}\omega_j - \vec{\omega}u_j]\right\}d\Gamma - \frac{1}{\nu}\int_{\Omega_i} [\vec{u}\,\omega_j - \vec{\omega}u_j] \cdot \vec{\nabla}u^*\,d\Omega, \tag{4}$$

where ω_j is the jth component of the velocity vector and $\vec{q}$ is the vorticity flux vector $q_j = \vec{n} \cdot \vec{\nabla}\omega_j$. Solution of the vorticity transport equations yields domain vorticity values in the final step of the BEM algorithm.

The mesh in the problem of the channel with bifurcation barrier is composed of hexahedral elements. Quadratic interpolation within the hexahedra is employed using standard 27 node Lagrangian domain elements, used for all the field functions as well as for the products of velocity and vorticity field components. On each face of the hexahedrons, discontinuous linear interpolations for the flux are used. All flux nodes are located within the boundary elements, none are located at corners and edges – thus the unit normal and the flux value are unambiguously defined in each flux node. In order to calculate the integrals, a Gaussian quadrature algorithm is used.

In order to set up a system of equations the source point is set to all function and flux nodes of all mesh elements. Each element is treated as an individual subdomain, thus a sparse system of equations is obtained. Compatibility boundary conditions are employed between subdomains. The sparse system of equations is solved using a least squares based iterative solver [17].

3.1.2. Single domain BEM

Computation of the boundary vorticity values from flow kinematics equation by applying the single domain BEM is crucial for obtaining divergence free computational results [19]. In order to obtain boundary vorticity values, we rewrite kinematics equation (3) into a tangential form by multiplying the system with a normal in the source point:

$$c(\vec{\vartheta})\overrightarrow{n(\vec{\vartheta})} \times \vec{u}(\vec{\vartheta}) + \overrightarrow{n(\vec{\vartheta})} \times \int_{\partial\Omega_i} \vec{u}\,\vec{\nabla}u^\star \cdot \vec{n}\,d\Gamma$$
$$= \overrightarrow{n(\vec{\vartheta})} \times \int_{\partial\Omega_i} \vec{u} \times [\vec{n} \times \vec{\nabla}]u^\star\,d\Gamma + \overrightarrow{n(\vec{\vartheta})} \times \int_{\Omega_i} [\vec{\omega} \times \vec{\nabla}u^\star]\,d\Omega. \tag{5}$$

The source point is set to all nodes on the exterior boundary of the domain, leading to a system of linear equations for the boundary vorticity values. The solution of this system is computed in each iteration of the nonlinear solution process until convergence is achieved. Since the system matrix remains unchanged through the whole nonlinear solution procedure, i.e. it does not depend on the flow variables, we perform the LU decomposition on the system matrix before the start of the nonlinear loop. Then, in each iteration of the nonlinear loop, the stored LU decomposition is used to obtain the boundary vorticity values.

3.2. Magnetic field computation

The magnetic field strength H_0 is varied by adjusting the distance between the magnets. The external magnetic field magnetizes the stainless steel 430 wires producing an inhomogeneous magnetic field in the bifurcating channel. Magnetization of the wires and magnetic spheres exhibits a nonlinear behaviour, thus H–M curves for wires and magnetic spheres are used (see [14] for details). According to the H–M curves the saturation magnetization of stainless steel wires is 1.38×10^6 A/m and that of magnetic spheres is 1.6×10^4 A/m.

Considering the cylindrical shape of the wires, the magnetic field strength $\vec{H}$ outside of the wires can be written as [20]

$$\vec{H} = \begin{pmatrix} 0 \\ 0 \\ H_0 \end{pmatrix} - \frac{M_w R^2}{2} \sum_{i=1}^{2} \frac{1}{r_i^4} \begin{pmatrix} 0 \\ 2[y - y_i][z - z_i] \\ [z - z_i]^2 - [y - y_i]^2 \end{pmatrix}, \tag{6}$$

where M_w is the magnetization of the wires, R the radius of the wires, r_i the distance from the centres of the wires and (y_i, z_i) the
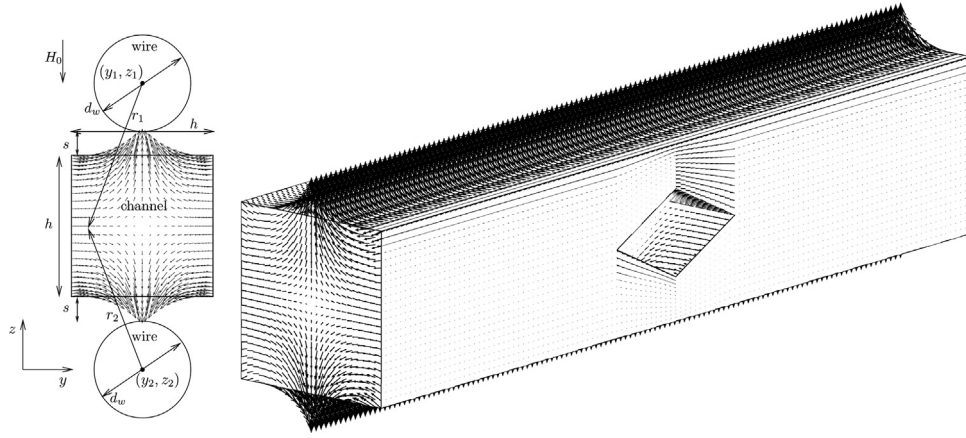
Fig. 2. Magnetic force vectors in the cross section of the channel (left) and isometric view on force vectors for a larger bifurcation barrier.

location of the centres of the wires. Analytical expression (6) for the magnetic field strength $\overrightarrow{H}$ is used in the computation of the Kelvin force acting on particles (Fig. 2), resulting in the following expression for the Kelvin force:

$$\overrightarrow{F}_m = \xi_m \mu_0 V_p \left[\chi_f - \frac{M_p}{H}\right][\overrightarrow{H} \cdot \overrightarrow{\nabla}]\overrightarrow{H} \qquad (7)$$

where ξ_m is the volumetric fraction of ferromagnetic material in the particle, in this case $\xi_m = 0.1245$. With known $\overrightarrow{H}$, the magnetic flux density $\overrightarrow{B}$ can be computed, which is equal to the magnetic field strength $\overrightarrow{H}$ times the magnetic permeability μ_0 in the region in which the field exists, $\overrightarrow{B} = \overrightarrow{H}\mu_0$. In the present study the magnetic flux density value has been varied in order to establish its effect on the magnetic particle behaviour i.e. the collection efficiency.

3.3. Particle tracking

A Lagrange based particle tracking model [14] was implemented in order to determine particle trajectories. The particles are considered as spherical with diameter d_p, mass m_p and density ρ_p. The mass of fluid encompassing the same volume as the particle is denoted by m_f. The equation of motion for small rigid spheres, adopted in the particle tracking algorithm, was proposed by Maxey and Riley [21]. Considering gravity, buoyancy, pressure gradient term, added mass term, drag (skin friction and form drag) and the magnetic force term, we may write this equation in the following form:

$$m_p \frac{d\overrightarrow{v}}{dt} = [m_p - m_f]\overrightarrow{g} + m_f \frac{D\overrightarrow{u}}{Dt} - \frac{1}{2}m_f\left[\frac{d\overrightarrow{v}}{dt} - \frac{d\overrightarrow{u}}{dt}\right]$$
$$- 3\pi d_p \rho_f \nu[\overrightarrow{v} - \overrightarrow{u}] - \xi_m \mu_0 V_p \left[\chi_f - \frac{M_p}{H}\right][\overrightarrow{H} \cdot \overrightarrow{\nabla}]\overrightarrow{H}, \qquad (8)$$

where $\overrightarrow{v}$ is the velocity of the particle and $\overrightarrow{u}$ is the fluid velocity. Here, $d/dt = \partial/\partial t + [\overrightarrow{v} \cdot \overrightarrow{\nabla}]$ represents the time derivative following the particle and $D/Dt = \partial/\partial t + [\overrightarrow{u} \cdot \overrightarrow{\nabla}]$ is the time derivative following the fluid element. The magnetic force term applies to the volumetric fraction of ferromagnetic material (ξ_m) and magnetic sphere magnetization M_p. The magnetic susceptibility of water is set to $\chi_f = -9 \times 10^{-6}$.

Eq. (8) is rewritten in non-dimensional form with H_0, u_0 and L being the characteristic magnetic field strength, the characteristic fluid velocity scale and characteristic problem length scale, respectively. With $\overrightarrow{H} \rightarrow \overrightarrow{H}/H_0$ $\overrightarrow{u} \rightarrow \overrightarrow{u}/u_0$, $\overrightarrow{v} \rightarrow \overrightarrow{v}/u_0$ and $t \rightarrow tu_0/L$ this results eventually in

$$\overrightarrow{a} = \frac{d\overrightarrow{v}}{dt} = \frac{A}{St}\{\overrightarrow{v}_s + [\overrightarrow{u} - \overrightarrow{v}]\} + \frac{3}{2}R\frac{\partial\overrightarrow{u}}{\partial t}$$

$$+ R\left\{\left[\overrightarrow{u} + \frac{1}{2}\overrightarrow{v}\right] \cdot \overrightarrow{\nabla}\right\}\overrightarrow{u} - \xi_m A\frac{\mu_0 H_0^2}{u_0^2 \rho_p}\left[\chi_f - \frac{M_p}{H}\right][\overrightarrow{H} \cdot \overrightarrow{\nabla}]\overrightarrow{H}, \qquad (9)$$

where the Stokes number is defined as

$$St = \frac{\rho_p d_p^2 u_0}{\rho_f 18\nu L}, \qquad (10)$$

the settling velocity is

$$\overrightarrow{v}_s = \frac{d_p^2}{18\nu u_0}\left[\frac{\rho_p}{\rho_f} - 1\right]\overrightarrow{g}, \qquad (11)$$

and the parameters R and A are set to

$$R = \frac{\rho_f}{\rho_p + \frac{1}{2}\rho_f} = 0.4897, \quad A = \frac{\rho_p}{\rho_p + \frac{1}{2}\rho_f} = 0.7552. \qquad (12)$$

In order to better understand the interaction of hydrodynamic and magnetic forces they act on a particle, we can define the magnetic pressure coefficient [22], which represents the importance of the magnetic pressure with respect to the dynamic pressure of the fluid phase as

$$C_{pm} = \frac{\mu_0 H_0^2}{u_0^2 \rho_f} \qquad (13)$$

Using the magnetic pressure coefficient, the final form of the equation governing the acceleration of the particles is

$$\overrightarrow{a} = \frac{d\overrightarrow{v}}{dt} = \frac{A}{St}\{\overrightarrow{v}_s + [\overrightarrow{u} - \overrightarrow{v}]\} + \frac{3}{2}R\frac{\partial\overrightarrow{u}}{\partial t}$$
$$+ R\left\{\left[\overrightarrow{u} + \frac{1}{2}\overrightarrow{v}\right] \cdot \overrightarrow{\nabla}\right\}\overrightarrow{u} - \xi_m RC_{pm}\left[\chi_f - \frac{M_p}{H}\right][\overrightarrow{H} \cdot \overrightarrow{\nabla}]\overrightarrow{H}, \qquad (14)$$

The non-dimensional magnetic force term is calculated based on the magnetic field strength (6) as

$$[\overrightarrow{H} \cdot \overrightarrow{\nabla}]\overrightarrow{H} = -\frac{M_w R^2}{2H_0}\sum_{i=1}^{2}\frac{1}{r_i^6}\begin{pmatrix} 0 \\ 2[y-y_i]\left[\frac{M_w R^2}{H_0} - 2[y-y_i]^2 + 6[z-z_i]^2\right] \\ 2[z-z_i]\left[\frac{M_w R^2}{H_0} - 6[y-y_i]^2 + 2[z-z_i]^2\right] \end{pmatrix}. \qquad (15)$$

With the acceleration of the particle given in Eq. (9) we may solve the particle equation of motion by employing the 4th order Runge–Kutta method [23]. We integrate the following six equations simultaneously:

$$\frac{dx}{dt} = v_x, \quad \frac{dv_x}{dt} = a_x, \quad \frac{dy}{dt} = v_y, \quad \frac{dv_y}{dt} = a_y, \quad \frac{dz}{dt} = v_z, \quad \frac{dv_z}{dt} = a_z \qquad (16)$$

The unknowns are the particle location (x, y, z) and particle velocity (v_x, v_y, v_z). Thus the initial particle location and velocity must be known. In order to calculate the acceleration contributions
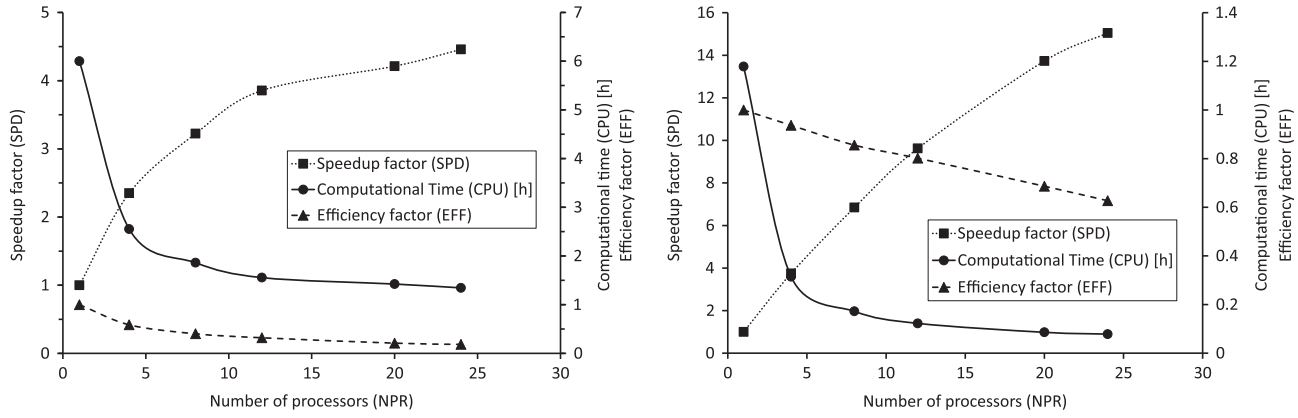
Fig. 3. Computational time (CPU), speedup and efficiency factor for different numbers of processors in the fluid flow solver (left) and particle tracking solver (right).

on the right-hand side, the velocity of the fluid, $\vec{u}$, has to be calculated at the location of the particle. The solution algorithm described in detail in Ravnik et al. [24] has been used.

3.4. Parallel computing

All the examples where calculated on the HPC CINECA IBM PLX-GPU cluster consisting of 300 nodes of different types. The system consists of 274 IBM X360M2 12-way compute nodes. Each one contains 2 Intel(R) Xeon(R) Westmere six-core E5645 processors (2.40 GHz), each node has 48 GB of memory. The calculation speedup and the efficiency test of the water flow with $Re = 1$ in a bifurcating channel were performed for fluid flow solver. The calculation mesh consists of $60 \times 12 \times 12$ domain elements. For particle tracking solver the corresponding fluid field was used and 10,000 particles tracked in magnetic field of $B_0 = 0.62$ T for a very short time 2.5 ms. In Fig. 3 the computational time (*CPU*), the speedup ($SPD = CPU(1)/CPU(NPR)$) and the efficiency ($EFF = SPD/NPR$) factor are presented for different numbers of processors (*NPR*). In the first part of fluid flow simulation only the kinematic equations are parallelized in the form that each processor handles its own part from the system of equation. The main goal of the parallelization of the kinematics fluid part is to resolve the high computer memory demands of the BEM code, therefore the moderate speedup is not a limiting factor. The second application of parallelization was used in the particle tracking, where the speed up of the parallel code is almost linear due to the consideration of a dilute suspension. Since particle–particle interactions are not considered, each processor handles its own share of particles and communication between processors is necessary only at the end of the simulation for writing the result file and not during the iterative time stepping.

4. Results and discussion

The flow field was computed for the 3.75 mm × 0.75 mm × 0.75 mm square cross sectional channel with bifurcation in the middle of the channel. The computational mesh consisted of $60 \times 12 \times 12$ domain elements having in total 186,792 nodes. On the solid walls the elastic particle bouncing boundary condition was prescribed except on the walls on the upper and lower parts of the channel where particles that hit the wall were considered as collected and removed from further tracking. The magnetic particle separation was solved for two different geometrical setups of the bifurcating barrier inside the straight channel: the larger $h_{bif} = h/2 = 0.375$ mm and the smaller $h_{bif} = h/8 = 0.09375$ mm (Fig. 1). The specific flow rates for each geometrical setup were

Table 1
Mean flow velocities used in simulations with corresponding Reynolds and Stokes number values.

u_0 (cm/s)	Re	St ($\times 10^{-6}$)
8	59.36	26.1
5	37.1	16.3
2.5	18.55	8.15
1.35	10.0	4.4

varied from $u_0 = 1.35$ cm/s to $u_0 = 8$ cm/s (Table 1). The third step in the numerical experiments was a variation of the magnetic flux density from $B_0 = 0.04$ T to $B_0 = 0.62$ T. For all three series of numerical experiments the collection efficiency ζ was determined in order to asses the influence of different parameters on the efficiency of the HGMS separation unit with bifurcating barrier. The collection efficiency defines the fraction of magnetic particles that enter the separation unit and become attached to the top and bottom channel walls.

It is important to note that with rising values of the *Re* number the recirculation zone after the barrier is increasing, therefore it needs to be checked if the flow at the outlet regains its fully developed state from the inlet of the channel, facilitating the use of periodic boundary conditions. A comparison of different flow fields for geometrically different HGMS devices with the highest prescribed velocity $u_0 = 1.35$ cm/s on the inlet is presented in Fig. 4. From these results we can see that the flow accelerates in the region above and below the barrier, and that the flow at the outlet of the segment (3.75 mm) is again fully developed. This allowed us to use the periodic boundary conditions in the next step where magnetic particle tracking was performed. In the case of periodic boundary conditions values of velocity and vorticity at the outlet were copied back to the inlet plane. In the same manner, particle positions at the outlet were used as inlet positions for the simulation of the next segment of the channel. In order to record the particles position history it is important to set the length of the segment prior to beginning of computations, since when a particle is tracked and reaches the outlet plane of the segment, its $y–z$ position in the flow as well as its velocity direction are stored and used as the boundary condition at the inlet (Fig. 5). The x position coordinate is computed according to the segment's number and relative position inside the segment. The advantage of the periodic boundary conditions is its capability to simulate particle tracking in a much longer channel, consisting of several in-line positioned bifurcating barriers.

Several electric currents were selected, which result in magnetic flux densities ranging between $B_0 = 0.04$ T and $B_0 = 0.62$ T. The corresponding magnetic pressure coefficients (Table 2),

computed for the system as a whole (13), clearly indicate the predominance of the magnetic force over hydrodynamic forces, although the local values of this coefficient do vary significantly. In all computed cases a total of 10,000 polystyrene magnetic spheres were tracked using the Lagrangian particle tracking algorithm. This number of particles was chosen in order to obtain representative statistics of collection efficiency without violating the dilute suspension assumption.

The final particles distribution in the case of larger and smaller bifurcations is shown in Fig. 6, from which we can see that the collection efficiency on the top and bottom walls is much higher for the case of the smaller bifurcation. From these results we can also observe the final particle positions at the outlet of the channel indicating that in the case of a larger bifurcation the particles distribution is wider than in the case of the smaller barrier size, where they are positioned mostly in the middle of the channel. This observation could be explained by the fact that in the case of the larger barrier the flow perturbation is larger, leading to stronger hydrodynamic forces. Improvement of the collection efficiency for the smaller bifurcation barrier size can be attributed to a prolonged exposure of the magnetic particles to the higher magnetic force field, obtained by redirecting the flow with particles towards the upper/lower walls, which are in the vicinity of the magnets. For lower flow rates, this effect is not decreased by

redirection of the flow field towards the center of the channel, which occurs in the divergent part of the channel, as the flow quickly regains its developed state. For higher flow rates, the formation of a weak jet could be observed in the divergent part of the channel, which increases the distance until the flow attains the developed state. Combined with the increase in strength of the hydrodynamic forces when increasing the flow rate this leads to a decrease of the collection efficiency of the channel with bifurcations.

Results for larger and smaller bifurcations, shown in Fig. 6, are also presented in terms of particle collection efficiency per distance ζ/x versus the separation channel length, Fig. 7. Particle collection efficiency is defined as the fraction of the number of magnetic particles that entered the separation unit and become attached to the top and bottom channel walls. From these results it is evident that the collection efficiency along the channel is much higher in the case of a smaller bifurcating barrier, whereas in the case of the larger bifurcation the efficiency is similar to the channel without bifurcation.

A comparison of different geometrical cases of HGMS units, presented in Figs. 8 and 9, shows particle collection efficiency ζ versus magnetic field flux B_0 for both geometrical cases of the bifurcation and for two different flow rates $u_0 = 1.35$ m/s ($Re = 10$) and $u_0 = 5.0$ m/s ($Re = 37.1$). In the case of the lower flow rate $u_0 = 1.35$ m/s ($Re = 10$) the collection efficiency is the largest in the case of the smaller barrier size, while in the case of the higher flow rate $u_0 = 5.0$ m/s ($Re = 37.1$) the largest collection efficiency is observed with the case of no bifurcation barrier [14]. This can be attributed to the fact that there is no redirection of the flow field in the narrow channel, which in the case of higher flow rates and the bifurcating channel decreases the collection efficiency. The decrease of the collection efficiency for larger bifurcation compared to the other two channel configurations is also attributed to the fact that in the channels above and under the bifurcation barrier flow velocities locally increase, and although particles approach the area of higher magnitude of Kelvin force, the time interval within which particles are exposed to these forces is not long enough to significantly alter the particle trajectories. Also, the
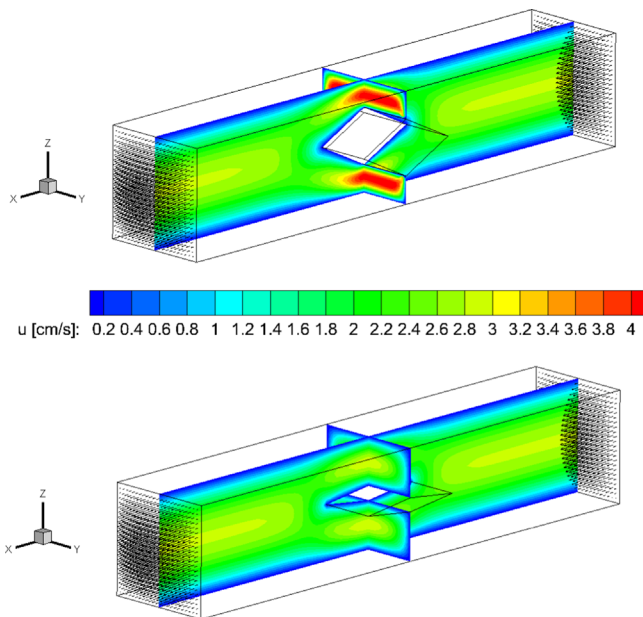

u [cm/s]: 0.2 0.4 0.6 0.8 1 1.2 1.4 1.6 1.8 2 2.2 2.4 2.6 2.8 3 3.2 3.4 3.6 3.8 4

Fig. 4. Flow field in segment (3.75 mm) of the channel for larger ($h_{bif} = h/2$) and smaller ($h_{bif} = h/8$) size of bifurcating barrier for the case $Re = 10$ ($u_0 = 1.35$ cm/s).

Table 2
Magnetic pressure coefficients C_{pm} for different magnetic flux densities B_0 used in simulations and corresponding Reynolds number values.

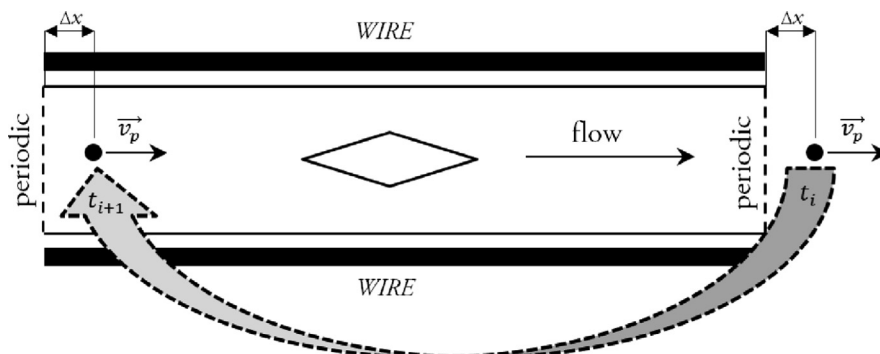| Re	B_0			
	0.04 T	0.12 T	0.32 T	0.62 T
10	6.75E+03	6.07E+04	4.32E+05	1.73E+06
18.55	1.97E+03	1.77E+04	1.26E+05	5.04E+05
37.1	4.92E+02	4.42E+03	3.15E+04	1.26E+05
59.36	1.92E+02	1.73E+03	1.23E+04	4.92E+04

Fig. 5. Periodic boundary conditions for magnetic particle tracking.
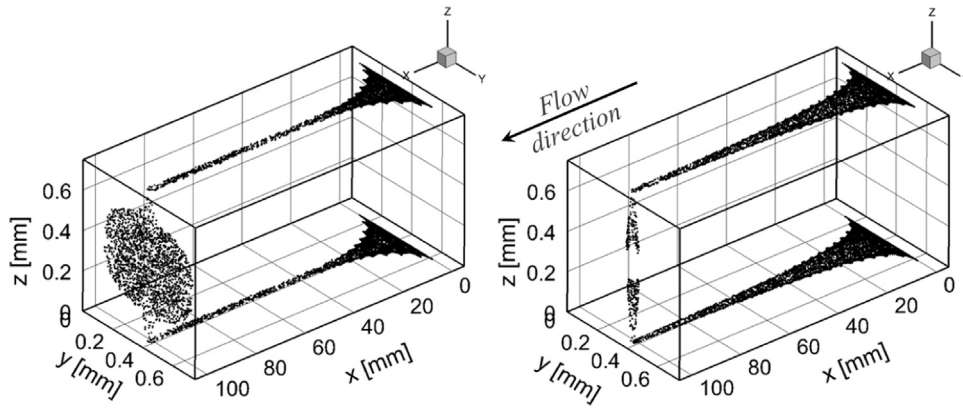
Fig. 6. Final particle positions for both geometrical cases of the channel with bifurcation (left – larger bifurcation ($h_{bif} = h/2$) and right – smaller bifurcation ($h_{bif} = h/8$)) for flow rate $u_0 = 1.35$ m/s ($Re = 10$) and magnetic field flux $B_0 = 0.62$ T.
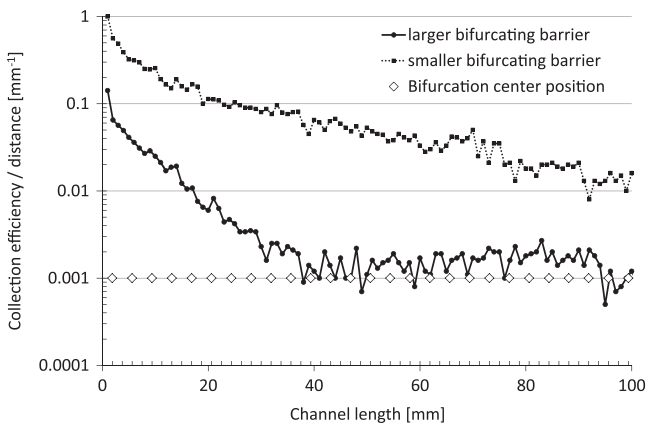

Fig. 7. Particle collection efficiency per distance ζ/x versus the separation channel length for the case $u_0 = 1.35$ m/s ($Re = 10$) and $B_0 = 0.62$ T for both geometrical cases of the channel with bifurcation.
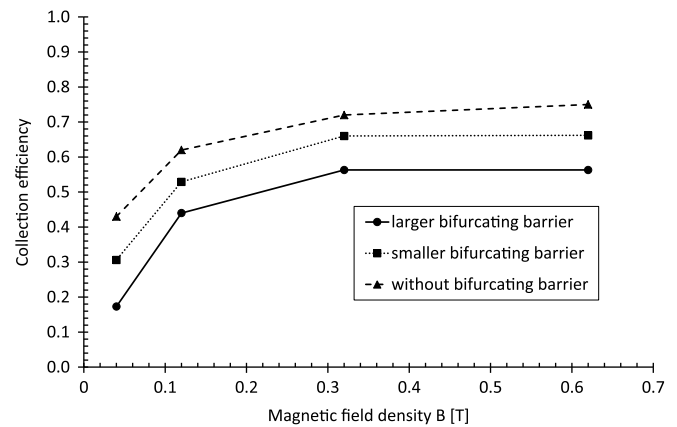

Fig. 9. Particle collection efficiency ζ versus magnetic field flux B_0 for $u_0 = 5.0$ m/s ($Re = 37.1$) for geometrical cases of the channel with and without [14] bifurcation.
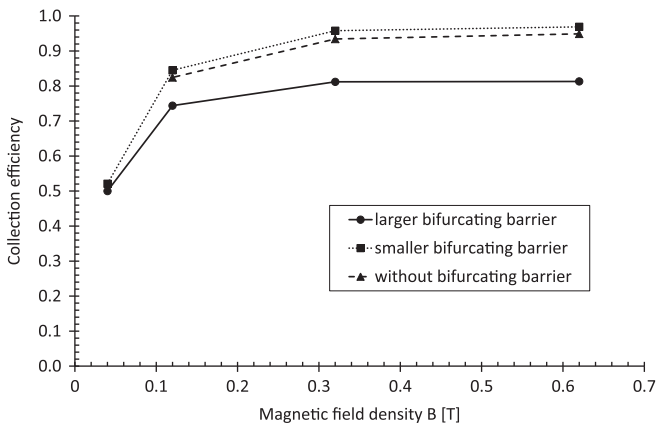

Fig. 8. Particle collection efficiency ζ versus magnetic field flux B_0 for $u_0 = 1.35$ m/s ($Re = 10$) for geometrical cases of the channel with and without [14] bifurcation.

particle Stokes number values in the selected cases are very small, this means that the particles tend to follow the flow field, the effect which is amplified in the regions of high velocities and low magnetic field flux.

The collection efficiency is in all simulations higher with increasing magnetic field flux and is limited with the saturation point of the particle magnetization characteristics [14], which occurs for the stainless steel 430 wire and the magnetic spheres

for $B_0 > 0.3$ T. An opposite behaviour occurs for the case of increasing flow rates presented in Fig. 10 for the case with smaller bifurcating barrier size. This relation is also exhibited for the case of larger bifurcating barrier size and also for the case without barrier [14]. With higher flow rates the collection efficiency is decreased, because of the larger inertial forces compared to the magnetic force acting on particles. These relations are also evident from Fig. 11 where collection efficiency versus flow rate for case with smaller bifurcating barrier is presented for different magnetic field fluxes. Fig. 12 presents also collection efficiency versus flow rate but for all geometrical cases of channel with and without [14] bifurcation for magnetic field flux $B_0 = 0.62$ T. Increasing the flow rate leads to a deterioration of the collection efficiency, as presented in Fig. 10 for the case with smaller bifurcating barrier size, although increasing the magnetic field flux up to the saturation point does improve separation to a certain extent. This relation can be also observed with the other two geometrical cases, including the channel with no bifurcation [14]. In Fig. 11 where the collection efficiency versus the flow rate for the case with smaller bifurcating barrier is presented, we can again observe the effect of saturation on the collection efficiency, as increasing the magnetic field flux from 0.32 T to 0.62 T does not lead to noticeable collection efficiency improvement. In Fig. 12, where the highest magnetic field flux was used, a clear advantage of the proposed channel design can be observed to exist in the range of flow rates up to 2 m/s, where the smaller bifurcation outperforms the original separation design.
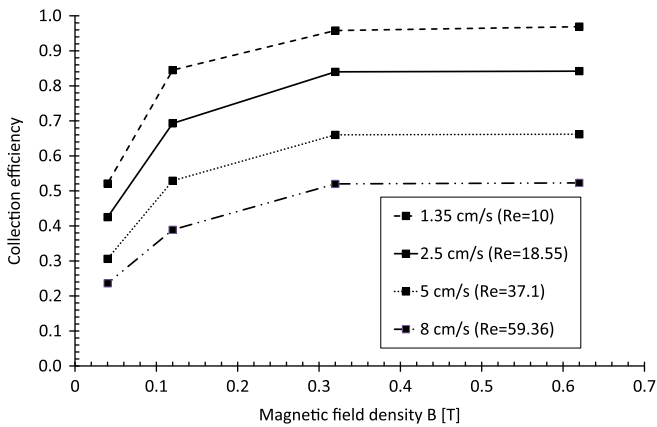
Fig. 10. Particle collection efficiency ζ versus magnetic field flux B_0 for the case with smaller bifurcating barrier ($h_{bif} = h/8$) and different flow rates.
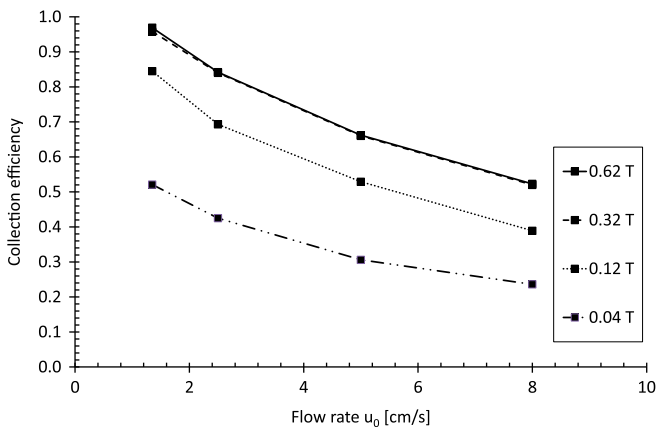

Fig. 11. Particle collection efficiency ζ versus flow rate for case with smaller bifurcating barrier ($h_{bif} = h/8$) and different magnetic field fluxes.
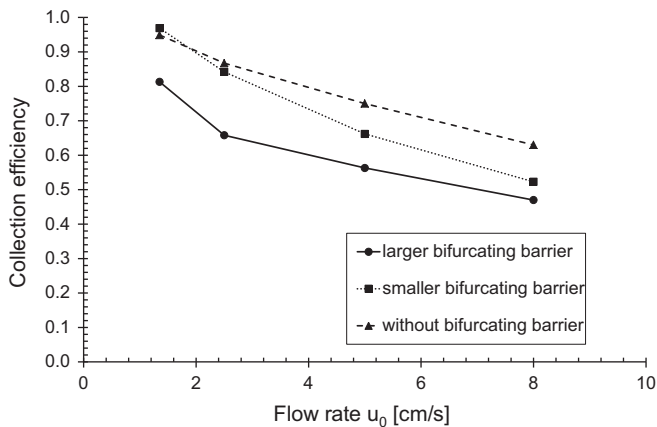

Fig. 12. Particle collection efficiency ζ versus flow rate for geometrical cases of channel with and without [14] bifurcation for magnetic field flux $B_0 = 0.62$ T.

5. Conclusions

The Boundary Element Method based 3D fluid flow simulation inside a high gradient magnetic separation channel with bifurcation was applied in order to study the collection efficiency of different channel designs. Due to the large aspect ratio of the separation channel, the segmentation based computational approach was developed. Within the Lagrangian particle tracking the Kelvin body force was included in order to be able to study the collection efficiency of the device. Starting from the original channel design, where a collection efficiency was negatively influenced by the existence of low magnetic forces in the middle of the channel, a new design with periodically positioned symmetric bifurcations was studied. Simulation results showed that increasing the size of the bifurcating barrier does not improve collection efficiency, as the efficiency was lower than in the case of the narrow channel without the bifurcation. On the other side, with a moderate size of the bifurcating barrier the collection efficiency can be improved, although the improvement is partly limited by the flow rate and magnetization saturation effects. The performed study shows that collection efficiency of a HGMS device can be improved by a careful design of the flow field, and shows potential for further improvements, especially in the case of viscous media such as blood under lower flow rates $Re < 10$ [16].

References

[1] Pankhurst Q, Connolly J, Jones S, Dobson J. Applications of magnetic nanoparticles in biomedicine. J Phys D: Appl Phys 2003;36:R167–81.
[2] Ying TY, Yiacoumi S, Tsouris C. High-gradient magnetically seeded filtration. Chem Eng Sci 2000;55:1101–13.
[3] Moeser GD, Roach KA, Green WH, Hatton TA. High-gradient magnetic separation of coated magnetic nanoparticles. AIChE J 2004;50:2835–48.
[4] Ditsch A, Lindenmann S, Laibinis PE, Wang D, Hatton TA. High-gradient magnetic separation of magnetic nanoclusters. Ind Eng Chem Res 2005;44: 6824–36.
[5] Svoboda J, Ross V. Particle capture in the matrix of a magnetic separator. Int J Miner Process 1989;27:75–94.
[6] Goleman R. Macroscopic model of particles capture by the elliptic cross-section collector in magnetic separator. J Magn Magn Mater 2004;272–276: 2348–9.
[7] Hatch G, Stelter R. Magnetic design considerations for devices and particles used for biological high-gradient magnetic separation (HGMS) systems. J Magn Magn Mater 2001;225:262–76.
[8] Tsutsui H, Ho C-M. Cell separation by non-inertial force fields in microfluidic systems. Mech Res Commun 2009;36:92–103.
[9] Liu T-Y, Hu S-H, Liu D-M, Chen S-Y, Chen I-W. Biomedical nanoparticle carriers with combined thermal and magnetic responses. Nano Today 2009;4(1): 52–65.
[10] Chen H, Kaminski M, Liu X, Xie Y, Mertz C, Torno M, et al. A novel human detoxification system based on nanoscale bioengineering and magnetic separation techniques. Med Hypotheses 2007;68:1071–9.
[11] Singh H, Laibinis P, Hatton T. Rigid, Superparamagnetic chains of permanently linked beads coated with magnetic nanoparticles. Synthesis and rotational dynamics under applied magnetic fields. Langmuir 2005;21:11500–9.
[12] Chiriac H, Moga A-E, Iacob G, Mungiu OC. Amorphous magnetic microspheres for biomedical applications. J Magn Magn Mater 2005;293(1):28–32.
[13] Plouffe BD, Nagesha DK, DiPietro RS, Sridhar S, Heiman D, Murthy SK, et al. Thermomagnetic determination of fe3o4 magnetic nanoparticle diameters for biomedical applications. J Magn Magn Mater 2011;323(17):2310–7.
[14] Ravnik J, Hriberšek M. High gradient magnetic particle separation in viscous flows by 3D BEM. Comput Mech 2013;51:465–74.
[15] Li X, Popel A, Karniadakis G. Blood plasma separation in y-shaped bifurcating microfluidic channels. Phys Biol 2012;9:1–12.
[16] Chen H, Kaminski MD, Rosengart AJ. 2D modeling and preliminary in vitro investigation of a prototype high gradient magnetic separator for biomedical applications. Med Eng Phys 2008;30:1–8.
[17] Ravnik J, Škerget L, Žunič Z. Combined single domain and subdomain BEM for 3D laminar viscous flow. Eng Anal Bound Elem 2009;33:420–4.
[18] Ravnik J, Škerget L, Žunič Z. Velocity-vorticity formulation for 3D natural convection in an inclined enclosure by BEM. Int J Heat Mass Transf 2008;51: 4517–27.
[19] Škerget L, Hriberšek M, Žunič Z. Natural convection flows in complex cavities by BEM. Int J Numer Methods Heat Fluid Flow 2003;13:720–35.

[20] Peeters H. Analysis and exploitation of field imperfections in magnetic resonance imaging [Ph.D. thesis]. Utrecht University; 2006.

[21] Maxey M, Riley J. Equation of motion for a small rigid sphere in a nonuniform flow. Phys Fluids 1983;26:883–9.

[22] Sobral Y, Cunha F. A stability analysis of a magnetic fluidized bed. J Magn Magn Mater 2003;258–259:464–7.

[23] Press WH, Teukolsky SA, Vetterling WT, Flannery BP. Numerical recipes—the art of scientific computing. 2nd ed. Cambridge, UK: Cambridge University Press; 1997.

[24] Ravnik J, Škerget L, Hriberšek M, Žunič Z. Numerical simulation of dilute particle laden flows by wavelet BEM–FEM. Comput Meth Appl Mech Eng 2008;197(6–8):789–805.